fibers

MDPI

Article

Parametric Influence of Yarn Microstructure on Coupled Heat and Moisture Transport

Wang Xu [1], Yunchu Yang [2] and Abdel-Fattah Seyam [2,*]

[1] Wilson College of Textiles, North Carolina State University, Raleigh, NC 27606, USA; wxu8@ncsu.edu
[2] School of International Education, Zhejiang Sci-Tech University, Hangzhou 310018, China; gary0577@zstu.edu.cn
* Correspondence: aseyam@ncsu.edu

Highlights

What are the main findings?

- A two-dimensional fiber-level finite element model was developed and validated against ISO 11092 sweating guarded hotplate measurements to predict isothermal water-vapor transport and evaporative heat flux in PET multifilament yarn arrays.
- Yarn packing factor was the dominant microstructural variable: increasing the packing factor from 0.45 to 0.55 reduced heat flux by about 27% and total moisture flux by about 26%, whereas denier per filament and filament number produced smaller but systematic effects.

What is the implication of the main finding?

- Packing factor is the primary yarn-level design lever for tailoring moisture resistance, vapor permeability, and evaporative heat-transfer performance in fibrous textile assemblies.
- Filament size and filament number can be used as secondary parameters to refine pore connectivity and tortuosity; low-packing yarns favor internal flow penetration, while highly packed yarns promote bypass-dominated transport.

Abstract

This study examines how yarn microstructure influences isothermal water-vapor transport and the associated evaporative heat loss under ISO 11092 skin-model conditions. Sweating guarded hotplate experiments were performed on PET yarn-array specimens to measure evaporative heat flux and moisture resistance. A fiber-level two-dimensional finite element model was then developed to reproduce the same boundary conditions and simulate transport through a PET fiber/air matrix. Using a full-factorial design, denier per filament, the number of filaments, and packing factor were varied independently, with multiple random filament arrangements used for each parameter combination to account for microstructural variability. The model reproduced the main experimental trends and gave predictions consistent with measured heat flux and moisture resistance for representative yarn configurations. Over the investigated design space, packing factor had the strongest influence: higher packing reduced heat and moisture flux and increased moisture resistance. Denier per filament and the number of filaments showed smaller but systematic effects, mainly through changes in pore connectivity and tortuosity. Statistical analysis indicated that main effects accounted for most response variation, while interaction effects were limited within the studied ranges. Flow-field results further showed a shift from internal flow penetration at low packing to bypass-dominated transport at high packing. These findings provide

Check for updates

Academic Editor: Catalin R. Picu

Received: 11 May 2026
Revised: 18 June 2026
Accepted: 10 July 2026
Published: 15 July 2026

Copyright: © 2026 by the authors. Licensee MDPI, Basel, Switzerland. This article is an open access article distributed under the terms and conditions of the Creative Commons Attribution (CC BY) license.

a validated framework for linking yarn-level structural parameters with heat–moisture transport performance in fibrous assemblies.

Keywords: heat and moisture transfer; finite element analysis; multiphysics; fibers

1. Introduction

Heat–moisture coupling governs how clothing removes metabolic heat and sweat from the body, thereby shaping thermal sensation and comfort. Poor vapor permeability leads to sweat accumulation and a sticky feeling, and the enclosed air layers and garment design modulate dry and evaporative heat loss across human body [1]. Because many functional garments are used in safety-critical or high-sweat contexts (protective wear, sports, healthcare), predictive tools for coupled heat and moisture transport are essential to rational textile design [2].

Classical and modern models have established the foundation for coupled transport in fibrous porous media. Early continuum theories described simultaneous heat and moisture diffusion through textiles [3]. Later studies incorporated additional physics such as sorption/desorption, phase change, airflow coupling, and radiative transfer, which achieved good agreement with selected experiments under specific environmental conditions [4–7]. However, many of these approaches represent textiles as homogeneous layers or use idealized pore geometries, which limits their ability to capture the effects of realistic yarn microstructure and local heterogeneity [6,7].

Beyond continuum formulations, meso- to fabric-scale simulations have examined how structure affects thermal transport. Representative unit-cell and meso-scale models have varied yarn spacing, crimp, and cross-section geometry while accounting for anisotropy and temperature-dependent properties, and have reproduced steady or transient temperature/heat-flux trends in woven and knitted assemblies [8–14]. These studies also indicate that apparent thermal properties can be influenced by test configuration effects such as lateral heat leakage, layer sequencing, and weave type, which complicates direct interpretation of measured thermal resistance and conductivity [14–16]. While valuable for fabric-level trends, many of these models simplify yarn microstructure to maintain computational tractability [9,11]. Moisture-centric studies complement thermal modeling by identifying key drivers of vapor transfer. Coupled transient heat–vapor simulations have quantified effects of porosity and fiber orientation in fibrous media, while experimental and numerical works emphasize that inter-fiber and inter-yarn vents often dominate vapor pathways and that pore shape and arrangement can alter effective transport and phase-change behavior [17–22]. Lolaki et al. [18] highlighted that inter-fiber and inter-yarn vents dominate vapor pathways and enumerated structural determinants of porosity (counts, twist, spinning type, weave). At a higher level, numerical and experimental works show that pore shape and arrangement substantially alter effective conductivity and phase-change behavior in porous media [19–22]. However, the underlying pore geometry is frequently idealized or represented through averaged parameters, and the direct role of stochastic pore topology inside a yarn is often not resolved explicitly.

Yarn-scale studies are crucial because yarn microstructure sets the pore topology through which heat and vapor move. Prior work linked filament count, porosity, and fiber volume fraction to effective conductivity and air permeability in multifilament polyester yarns, though often assuming parallel, regularly packed fibers and focusing on dry conditions [23]. Circular cross-sections and idealized packing have also been used to model coupled transport in woven structures [24]. Experiments on knitted and woven fabrics

show that yarn parameters (linear density, twist, yarn construction) affect thermal resistance and vapor permeability, and statistical approaches relate macroscopic fabric descriptors (thickness, cover, pore size) to vapor transmission, although some datasets report limited sensitivity to twist or packing within the tested ranges [25–27]. Related studies on liquid moisture transport further demonstrate that yarn fineness and construction route reorganize capillary pathways and change wetting and wicking behavior [28,29]. In engineered moisture-management textiles, modeling and testing have validated quick-dry performance, but many simulations treat fabrics as isotropic porous media or rely on macro-averaged descriptions rather than explicit yarn microstructure [30,31]. More recently, random-geometry filament-yarn models highlighted how stochastic pore connectivity and tortuosity can create spatially heterogeneous transport fields; however, many such analyses emphasize thermal conduction under idealized conditions and do not systematically treat coupled moisture transport [32–36].

Many models homogenize at the fabric scale, enforce periodic or ideal fiber packing, or neglect realistic yarn microstructure to keep computations tractable [6,9,11,23,31,34]. These simplifications can misrepresent transient transport and local phase-change phenomena, especially when pore networks are irregular and moisture–heat coupling is strong [9,19–22]. Moreover, even when structural parameters are varied, they are often adjusted at fabric- or yarn-aggregate levels without explicitly resolving randomly distributed fibers and the resulting stochastic pore topology inside a yarn cross-section [8,9,13,23].

The objective of this study is to develop and utilize a two-dimensional, fiber-level finite element model representing a linear continuous fibrous assembly to: (1) simulate isothermal water-vapor transport and the associated evaporative heat flux through a PET fiber/air matrix, with transport properties validated against the ISO 11092-Ret standard [37]; (2) conduct a comprehensive parametric study by systematically and independently varying the number of filaments (Nf), the packing factor (φ), and the denier per filament (dpf), where Nf is the number of individual filaments in one multifilament yarn, φ is the fraction of the yarn cross-sectional area occupied by fibers, and dpf is the linear density of an individual filament; and (3) quantify the relative influence of each of these structural parameters on the resulting heat flux and moisture transport characteristics. Smooth PET multifilament yarns were selected as controlled model substrates to isolate the effects of denier per filament, the number of filaments, and packing factor. The yarn-array specimens are not intended to represent finished fabrics or garments directly; instead, they provide a reproducible yarn-level basis for future multi-level simulations of woven structures. By explicitly resolving random microstructure at the fiber scale and quantifying parameter sensitivities, this work supplies a physically grounded bridge between microstructural design variables and macroscale thermal–moisture comfort performance in functional textiles. The novelty of this work lies in its use of a computationally efficient two-dimensional finite element framework to bridge the gap between over-simplified 1D models and computationally expensive 3D models, providing clear, quantitative design principles for engineering linear fibrous assembly as foundation effort for developing generalized models of yarn-based fibrous structures with tailored thermophysiological comfort properties.

2. Materials and Methods

2.1. Materials and Specimen Preparation

Fully drawn (FDY) PET filament yarns supplied by Unifi, Inc. (Greensboro, NC, USA) were used to prepare all test specimens. Two yarn types were included: Repreve PET and a Repreve/Ciclo blend. Repreve® is a trademarked recycled PET performance fiber/yarn platform of Unifi, Inc., and Ciclo® is a trademarked additive technology incorporated into synthetic fibers, including polyester. In terms of the heat and moisture transport considered

in this study, both yarn types were treated as PET-based multifilament yarns with broadly similar low-hygroscopic behavior to conventional PET filament yarns. The main differences from conventional virgin PET are the recycled feedstock origin of Repreve PET and the additional Ciclo additive technology in the Repreve/Ciclo blend. The yarns differed in the number of filaments and linear density, and they were further processed to produce test specimens with controlled yarn density, twist level, and packing factor. The selected specimens, which were chosen to match the simulation parameters as closely as possible, are listed in Table 1. In this study, the number of filaments Nf refers to the number of individual filaments in one multifilament yarn. The multifilament yarn linear density is reported in denier (g/9000 m). Denier per filament (dpf) was calculated by dividing the multifilament yarn denier by the number of filaments. The yarn-array density refers to the number of multifilament yarns per meter in the prepared array specimen. The yarn array was used to isolate yarn-level vapor and heat transport under SGHP boundary conditions before adding fabric-scale variables such as weave architecture, yarn crimp, and inter-yarn structure. Therefore, the prepared specimens should be interpreted as controlled model substrates rather than end-use textile products.

Table 1. PET multifilament yarn and yarn-array specimen specifications after sample warping.

Yarn Type	Number of Filaments in One Yarn (Nf)	Multifilament Yarn Linear Density in Denier (g/9000 m)	Ends Density in Yarn Array (Yarns/m)	Twist per Meter	Packing Factor
FDY Repreve	72	150	3200	0	0.55
	72	75	5200	0	0.43
FDY Repreve/Ciclo	48	150	5000	600	0.51
FDY Repreve	72	150	5000	600	0.52
	72	75	7200	1200	0.55

As shown in Table 1, the Repreve yarns include 72-filament yarns with nominal linear densities of 150 and 75 denier. The Repreve/Ciclo yarn is a 48-filament yarn with a nominal linear density of 150 denier. For each yarn type, multiple configurations were prepared by varying yarn density (3000–7800 yarns/m), twist per meter (0, 600, and 12,00 turns/m), and packing factor (0.35–0.55). These combinations were selected to cover both low- and high-packing conditions and to include untwisted and twisted states.

All yarns were received as packages and processed in-house to prepare yarn arrays for the heat flux and moisture resistance measurements. To control the array geometry, each yarn type was first wound side-by-side on a ruler under the same tension condition used in sample preparation, and its average width was measured. This measured width was then used to determine the required end density and to set the spacing on the sample warper for each target yarn density listed in Table 1. The measured yarn width and thickness were further used to calculate the packing factor reported in Table 1 using the following equation:

$$\text{Packing factor} = \frac{N_f\, A_f}{A_{\text{ellipse}}}, \tag{1}$$

where N_f is the number of filaments, A_f is the circular cross-sectional area of a single filament, and A_{ellipse} is the area of the elliptical yarn cross-section.

2.2. Experimental Measurement

Moisture resistance was measured using a sweating guarded hot plate (SGHP) following ISO 11092 (R_{et}), with the specimen prepared as a yarn array. A schematic of the test principle and layer arrangement is shown in Figure 1. The system consists of a temperature-

controlled porous test plate located inside a climatic chamber, and a surrounding guard ring that helps maintain one-dimensional heat and moisture transfer through the specimen.

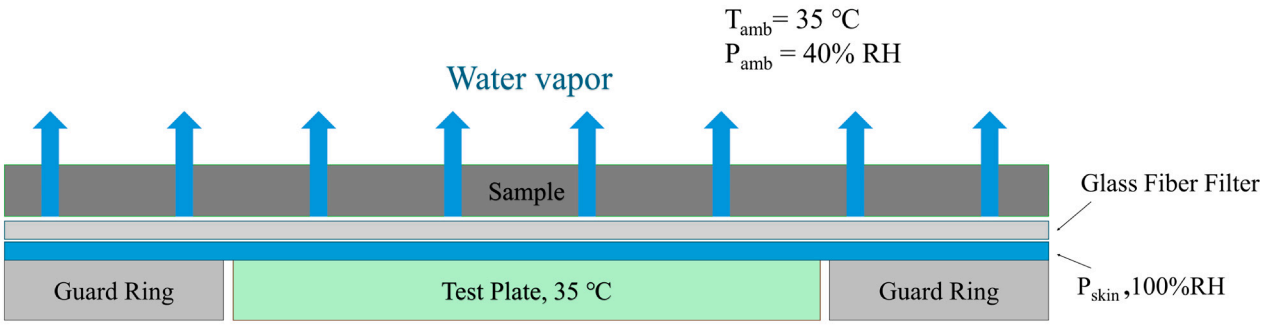


Figure 1. Schematic diagram of thermal resistance and moisture resistance tester (SGHP).

During testing, the porous test plate was maintained at 35 °C, which represents the skin-side temperature. The chamber air temperature was also set to 35 °C, and the ambient relative humidity was controlled at about 40%. A glass-fiber filter was placed on the plate surface. This filter allows water-vapor to pass while preventing liquid water from directly contacting the specimen. Water supplied beneath the porous plate generated a saturated vapor condition at the plate side (≈100% Relative Humidity (RH)). The ambient side remained at 40% RH. This vapor pressure difference drove water-vapor transport upward through the filter and the yarn-array specimen, as indicated by the arrows in Figure 1. The latent heat loss associated with evaporation and vapor transport was balanced by electrical heating of the plate, which was used to quantify the moisture resistance.

Before preparing the yarn-array specimens, the apparent yarn width and thickness of each yarn configuration were measured. Each yarn was wound repeatedly and side-by-side on a ruler, and the average yarn width was calculated from the total occupied width divided by the number of yarn wraps. The apparent thickness of the wound yarn was measured using a vernier caliper. The measured average width was used to determine the target yarn-array density and the corresponding spacing on the sample warper. The measured width and thickness were also used to approximate the yarn-bundle envelope for packing-factor calculation. These measurements represent the apparent yarn geometry under the preparation condition rather than a microscopic reconstruction of the exact filament-level cross-section.

The yarn specimens shown in Figure 2 were prepared as warped yarn arrays, as described in Section 2.1, and mounted on rigid rectangular frames to maintain the prescribed tension and geometry during testing. Figure 2b shows a representative framed yarn-array specimen, in which multiple PET multifilament yarns were arranged in parallel to form a controlled specimen layer for SGHP testing. Based on the average yarn width measured beforehand, the corresponding target end density was calculated and then used to set the spacing on the sample warper for each yarn configuration. The yarns were wound onto the frames using a sample warper under uniform tension and aligned as parallel as possible to minimize overlap and local spacing variation. The use of the sample warper was intended to produce a controlled yarn-array density and to minimize larger-scale coverage variation across the active test area. The yarns were arranged as closely as possible according to the target end density, but the specimen should still be regarded as a discrete yarn array rather than a continuous fibrous sheet. Therefore, small residual inter-yarn gaps were unavoidable because of the finite yarn cross-sectional width and thickness, local yarn deformation under tension, and minor spacing variations during warping. For each configuration, the framed array was placed horizontally on the SGHP test plate (Figure 2a). The array was centered so that the yarn region fully covered the active test area, and the yarns were in full contact

with the glass-fiber filter. After the specimen was installed, the system was operated under closed-loop control of the plate temperature until steady state was reached. In steady state, water vapor is transported from the saturated region at the plate side (≈100% RH) to the lower vapor pressure in the ambient air. The corresponding latent heat loss is balanced by electrical heating of the plate to maintain the target surface temperature. This setup is commonly referred to as a "skin model" because it reproduces evaporative heat loss and water-vapor transport near the human skin surface.



Figure 2. Experimental setup and specimen: (**a**) SGHP test apparatus and (**b**) representative framed yarn-array specimen prepared from parallel PET multifilament yarns for thermal–moisture transport measurements.

According to ISO 11092, the moisture resistance, R_{et} ($Pa \cdot m^2 \cdot W^{-1}$), is defined as the water-vapor pressure drop across the specimen divided by the corresponding evaporative heat flow through the specimen. It is calculated as

$$R_{et} = \frac{(P_{skin} - P_{amb})}{\frac{Q}{A}} \quad (2)$$

where P_{skin} (Pa) is the water-vapor pressure at the surface of the test plate, P_{amb} (Pa) is the ambient water-vapor pressure, Q (W) is the electrical heating power supplied to the plate at steady state, and A (m^2) is the effective test area.

The saturation vapor pressure was obtained from the plate temperature T_{skin} and the chamber air temperature T_{amb} using an empirical expression:

$$P_{sat}(T) = 133.3 \times 10^{(8.10765 \frac{1750.29}{235+T})} \quad (3)$$

with T in °C. The vapor pressures on the plate side and ambient side were then computed as

$$P_{skin} = P_{sat}(T_{skin}) \quad (4)$$

$$P_{amb} = RH \cdot P_{sat}(T_{amb}) \quad (5)$$

where RH is the ambient relative humidity expressed as a fraction.

Water-vapor permeability W_d ($g \cdot m^{-2} \cdot W^{-1} \cdot Pa^{-1}$) can then be obtained from the measured R_{et} as

$$W_d = \frac{1}{R_{et} u_t} \quad (6)$$

where u_t is the latent heat of evaporation of water at T_{skin}. For $T_{skin} = 35$ °C, $u_t \approx 0.627$.

For each yarn array configuration, at least three independent measurements were conducted. In each run, the system was allowed to reach steady state before Q, T_{skin}, and the chamber conditions were recorded. The moisture resistance, heat flux, and water-vapor permeability reported in this work are the averages of the repeated measurements for each configuration.

2.3. Creation of Finite Element Model

To quantify how yarn microstructure affects coupled heat and moisture transport, a two-dimensional fiber-resolved finite element model was developed in COMSOL Multiphysics 6.3 (COMSOL AB, Stockholm, Sweden) and evaluated using a full-factorial design with three independent variables: denier per filament, yarn packing factor, and the number of filaments. Table 2 summarizes the factor levels. The dpf was set to 1, 2, and 3. The number of filaments Nf included 48, 72, 96, and 144. The packing factor φ included 0.45, 0.50, and 0.55. Combining these levels yields $3 \times 4 \times 3 = 36$ unique parameter sets, which cover both fine and coarse filaments, low to high number of filaments, and moderate to dense packing states.

Table 2. Factor levels and simulation design summary.

Variable	Levels
Denier per filament	1, 2, 3
Number of filaments	48, 72, 96, 144
Packing factor	0.45, 0.5, 0.55
Total run	36 (3 × 4 × 3)
Random replicas per run	20
Total replicas	720

For each run, 20 random replicas were generated to represent random variations in filament arrangement within a yarn while keeping the same (dpf, Nf, φ) values as filament arrangement in the yarn cross-section varies due to migration caused by twisting the yarn. This randomization reflects the geometric variability caused by filament migration during yarn twisting. In total, 720 finite element simulations were performed, corresponding to 36 parameter sets and 20 replicas per set. The repeated replicas allowed the model to distinguish systematic effects of yarn structural parameters from run-to-run geometric randomness.

Table 3 lists the 36 base models (Model ID 1–36) and their corresponding inputs and geometric descriptors. Each Model ID is defined by a unique combination of dpf, Nf, and φ. The yarn denier was determined by the product of the number of filaments and denier per filament, i.e., yarn denier = dpf × Nf. The fiber diameter was calculated for each dpf level (e.g., 0.010, 0.014, and 0.018 mm for dpf = 1, 2, and 3, respectively, as shown in Table 3). For a fixed (dpf, Nf), the yarn diameter varies with packing factor: higher packing factor corresponds to a smaller yarn diameter, reflecting a denser cross-section. These geometric parameters were used to construct the cross-sectional model for the coupled heat–moisture simulations, and the Model ID provides a direct mapping between the design variables and the resulting yarn geometry.

Using the factor levels and the derived geometric parameters in Tables 1 and 2, the 2D cross-sectional model and boundary conditions are shown in Figure 3. A two-dimensional representation is adopted as an effective approximation because the SGHP boundary conditions are uniform along the specimen length and the cross-sectional pore network is expected to strongly influence transport resistance. Although the yarns are twisted, the present model approximates the microstructure using an equivalent representative cross-section that reflects the target packing state. In the model, individual filaments are

assumed as uniform circles embedded in an air domain. A rectangular outer domain is used so that the top and bottom edges can be assigned directly as the moisture inlet and outlet boundaries. The circular cross-section model was adopted as an idealized equivalent geometry for the full-factorial analysis. This simplification allowed dpf, the number of filaments, and packing factor to be varied systematically under a consistent modeling framework. It does not imply that all experimental yarns, especially untwisted and twisted multifilament yarns, have identical circular bundle cross-sections. In real specimens, the yarn-bundle envelope can vary with twist, tension, and packing state. Therefore, an elliptical cross-section model derived from our previous study and based on measured yarn width and thickness was also included in the validation comparison to evaluate the influence of using measured specimen geometry relative to the simplified circular model.

Table 3. Summary of yarn microstructure and geometric parameters for the 36 models.

Model ID	Dpf	Nf	φ	Yarn Denier	Fiber Diameter (mm)	Yarn Diameter (mm)
1	1	48	0.45	48	0.010	0.095
2	1	48	0.5	48	0.010	0.087
3	1	48	0.55	48	0.010	0.081
4	1	72	0.45	72	0.010	0.116
5	1	72	0.5	72	0.010	0.107
6	1	72	0.55	72	0.010	0.099
7	1	96	0.45	96	0.010	0.134
8	1	96	0.5	96	0.010	0.123
9	1	96	0.55	96	0.010	0.115
10	1	144	0.45	144	0.010	0.164
11	1	144	0.5	144	0.010	0.151
12	1	144	0.55	144	0.010	0.140
13	2	48	0.45	96	0.014	0.134
14	2	48	0.5	96	0.014	0.123
15	2	48	0.55	96	0.014	0.115
16	2	72	0.45	144	0.014	0.164
17	2	72	0.5	144	0.014	0.151
18	2	72	0.55	144	0.014	0.140
19	2	96	0.45	192	0.014	0.189
20	2	96	0.5	192	0.014	0.174
21	2	96	0.55	192	0.014	0.162
22	2	144	0.45	288	0.014	0.232
23	2	144	0.5	288	0.014	0.213
24	2	144	0.55	288	0.014	0.198
25	3	48	0.45	144	0.018	0.164
26	3	48	0.5	144	0.018	0.151
27	3	48	0.55	144	0.018	0.140
28	3	72	0.45	216	0.018	0.201
29	3	72	0.5	216	0.018	0.185
30	3	72	0.55	216	0.018	0.172
31	3	96	0.45	288	0.018	0.232
32	3	96	0.5	288	0.018	0.213
33	3	96	0.55	288	0.018	0.198
34	3	144	0.45	432	0.018	0.284
35	3	144	0.5	432	0.018	0.261
36	3	144	0.55	432	0.018	0.243

To quantify the geometric limitation associated with twist, the filament helix angle was estimated for the twisted validation specimens using $\tan \theta = 2\pi rT \approx \pi DT$, where θ is the filament helix angle, r is the filament radial position, D is the yarn diameter, and T is

the twist level in turns per meter. For the two 600 turns/m validation cases mapped to Models 26 and 17, D = 0.151 mm, giving tan θ = 2.85 and θ ≈ 70.6°. For the 12,000 turns/m case mapped to Model 6, D = 0.099 mm, giving tan θ = 3.73 and θ ≈ 75.0°. These estimates indicate that filament helicity is significant in the twisted specimens. Therefore, the present model should be interpreted as an effective two-dimensional cross-sectional approximation; it captures statistical variation in random filament placement through 20 replicas but does not explicitly resolve the additional three-dimensional pathway length and pore connectivity caused by twist.

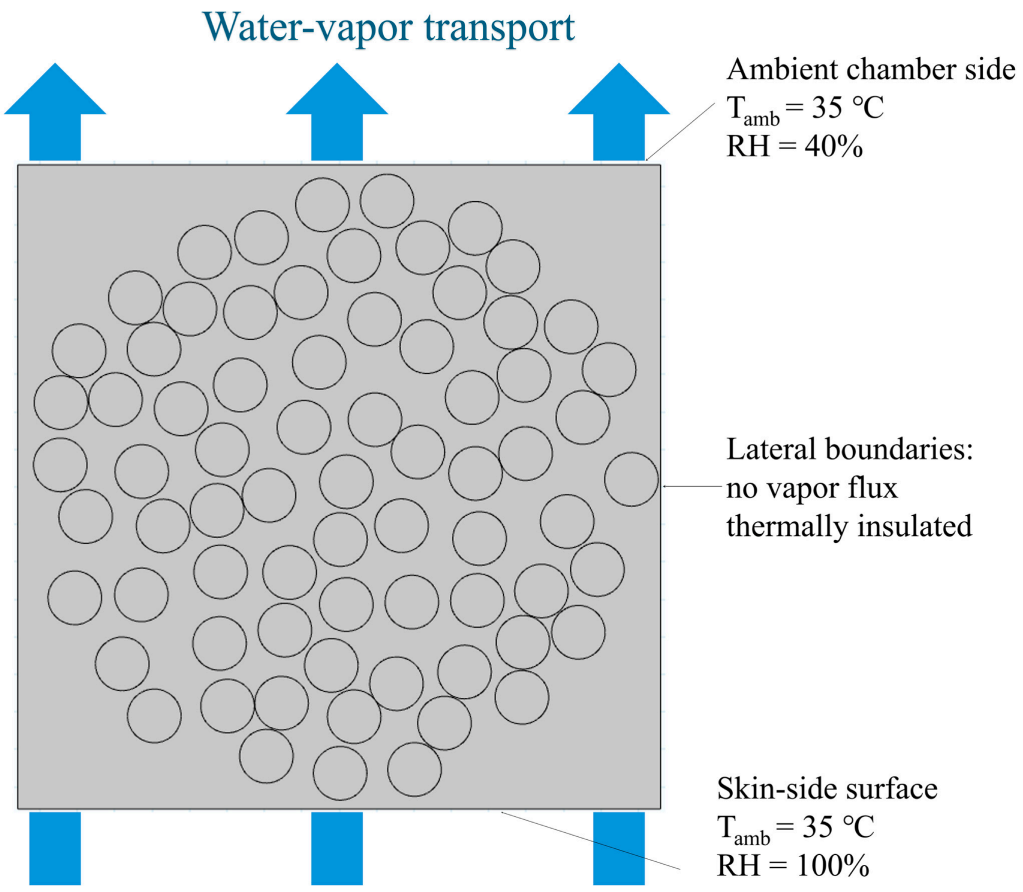


Figure 3. Schematic of the idealized two-dimensional fiber-level COMSOL Multiphysics model showing the PET yarn cross-section and imposed water-vapor transport boundary conditions (upward vapor flux).

Thermal boundary conditions followed the experimental "skin model." The lower boundary was prescribed at the plate (skin-side) temperature, T_{skin} = 35 °C, and the upper boundary was set to the same ambient air temperature, T_{amb} = 35 °C. The lateral boundaries were thermally insulated. The initial temperature in the entire domain was set to 35 °C. throughout the domain. Because both thermal boundaries were maintained at the same temperature, the model represents an isothermal vapor-transport condition.

For the laminar flow module, the PET fiber boundaries were treated as solid walls. For the Transport of Diluted Species module, the PET fiber boundaries and lateral boundaries were assigned no-flux boundary conditions for water vapor because PET was assumed to be hydrophobic and impermeable to vapor transport in the present model. The lower moisture boundary was prescribed as the evaporation side at 100% RH, and the upper boundary was prescribed as the ambient chamber side at 40% RH. The initial water-vapor concentration was set to the ambient value. At 35 °C, the saturated concentration is about 2.194 mol·m^{-3},

and the ambient concentration at 40% RH is 0.8776 mol·m^{-3}. These conditions match the driving force used in the SGHP measurements.

Water-vapor transport through the yarn array was driven by the imposed vapor-pressure difference between the saturated skin-side boundary and the ambient chamber boundary. Because both the lower and upper thermal boundaries were maintained at 35 °C, no macroscopic temperature gradient was imposed across the model domain. Therefore, the present model represents an isothermal evaporative transport condition rather than a non-isothermal heat-transfer problem driven by a temperature gradient. In this framework, the heat-transfer quantity of interest is the latent evaporative heat flux associated with water-vapor transport, which corresponds to the heat supplied by the sweating guarded hot plate to maintain the plate temperature during evaporation. The evaporative heat flux was calculated from the simulated water-vapor mass flux as

$$q''_{evap} = \dot{m}''_v h_{fg} \tag{7}$$

where q''_{evap} is the evaporative heat flux, $\dot{m}''_v$ is the water-vapor mass flux, and h_{fg} is the latent heat of evaporation of water at 35 °C. Thus, the coupling considered in this study is an isothermal latent heat–moisture coupling, not a temperature-gradient-driven heat-transfer process. The PET filaments and the surrounding humid air were treated as continua, each with its own thermal properties. Water vapor was modeled as a dilute species in air because, at 35 °C, the saturated vapor content corresponds to only a few percent of the gas mixture. Under this condition, humid air was approximated as a binary mixture with water vapor as the solute and dry air as the solvent.

Based on the operating principle of the sweating guarded hot plate (SGHP), the experimental process involves coupled heat transfer and water-vapor transport. Because the temperature difference across the specimen was minimal under the present testing condition, radiative heat transfer was neglected. The model was treated as a coupled PET fiber/air system, in which heat transfer occurs in both the solid fiber phase and the surrounding humid-air phase, while water vapor is transported through the air-filled pore space.

Heat transfer in the PET fiber domains was governed by Fourier's law and the solid heat transfer equation:

$$\vec{q} = -k\nabla T \tag{8}$$

$$\rho C_p \frac{\partial T}{\partial t} = \nabla \cdot (k\nabla T) + Q \tag{9}$$

where ρ is the density of the solid, C_p is the specific heat capacity, T is temperature, t is time, q is the conductive heat flux, Q is the volumetric heat source, and k is the thermal conductivity.

Heat transfer in the air domain was described by the heat-transfer equation for a moving fluid:

$$\rho' {C_p}' \frac{\partial T}{\partial t} + \rho' {C_p}' \vec{u} \cdot \nabla T + \nabla \cdot \vec{q}' = Q' \tag{10}$$

$$\vec{q}' = -k'\nabla T \tag{11}$$

where ρ', ${C_p}'$, k', and $\mathbf{q}'$ are the density, specific heat capacity, thermal conductivity, and conductive heat flux of the humid-air phase, respectively, and $\mathbf{u}$ is the gas velocity.

Moisture transport was modeled using the Transport of Diluted Species formulation. Under the testing condition of 35 °C, the saturated water-vapor content is small relative to

the air phase; therefore, humid air was treated as a gas mixture in which water vapor is transported as a dilute species in air. The diffusive flux of water vapor follows Fick's law:

$$\vec{J}_i = -D_i \nabla c_i \tag{12}$$

where J_i is the diffusion flux of water vapor, D_i is the diffusion coefficient of water vapor in air, and c_i is the water-vapor concentration. The general transient convection-diffusion equation is:

$$\frac{\partial c_i}{\partial t} + \vec{u} \cdot \nabla c_i + \nabla \cdot \vec{J}_i = R_i \tag{13}$$

where R_i is the source or sink term. In the present simulations, no internal vapor generation or consumption was prescribed in the air domain, and the steady-state solution was obtained under the imposed boundary humidity conditions.

The gas flow in the air-filled pore space was described using the continuity and momentum conservation equations for laminar flow:

$$\rho \nabla \cdot \vec{u} = 0 \tag{14}$$

$$0 = -\nabla p + \mu \nabla \cdot \left[\nabla \vec{u} + \left(\nabla \vec{u} \right)^T \right] + \vec{F} \tag{15}$$

where p is pressure, μ is the dynamic viscosity of the gas phase, **F** is the body-force term, and the superscript T denotes the transpose. In the present model, the PET fibers were treated as solid domains for heat transfer and as impermeable solid obstacles for moisture transport, while water-vapor transport occurred only through the connected air-filled pore space.

The air/fluid properties and water-vapor transport parameters used in the present model were adopted from the experimentally validated parameter set reported in our previous study [24]. No additional empirical fitting parameters were introduced in the present study; the SGHP experimental results were used only for validation of the yarn-level model response.

The present model focuses on isothermal water-vapor transport through the air-filled pore network in a PET fiber/air matrix. Vapor sorption into PET was not explicitly included because PET is a low-hygroscopic fiber. Reported moisture-regain values for polyester are approximately 0.4% under standard textile conditions [38]. Therefore, for the present steady-state vapor-transport analysis, moisture storage in the PET phase was considered secondary compared with vapor transport through the pore space. Condensation at fiber surfaces was also excluded. Because both boundaries were maintained at 35 °C and the imposed vapor conditions ranged from 40% RH at the upper boundary to 100% RH at the lower boundary, the local vapor pressure in the model was not expected to exceed the saturation vapor pressure at 35 °C. Therefore, supersaturation and surface condensation were not activated under the simulated conditions. Surface mass-transfer resistance at the external boundaries was not modeled explicitly. Instead, the lower and upper boundaries were prescribed as vapor-concentration boundaries corresponding to the SGHP saturated plate side and ambient chamber side, respectively. This formulation represents an ideal boundary condition and focuses the analysis on internal pore-network resistance within the yarn cross-section. Thus, the model predictions should be interpreted within the scope of prescribed boundary concentrations, negligible PET sorption, no condensation, and no explicitly resolved external mass-transfer boundary layer.

For each parameter set (dpf, Nf, φ), a yarn cross-section was generated by placing Nf circular filaments with a radius determined by the filament size (consistent with the dpf level). To control the packing state, filament centers were first generated inside a circular yarn boundary that represents the target yarn cross-section. Filament positions

were random, but a non-overlap constraint was enforced. The yarn radius was selected to satisfy the packing factor definition.

$$\varphi = \frac{N_f \pi r_f^2}{\pi R_y^2}, \tag{16}$$

so that packing factor is controlled by Nf, filament radius r_f, and yarn radius R_y. After a valid filament distribution was obtained, the circular yarn boundary was removed. This step avoids meshing difficulties associated with an additional internal boundary. A rectangular air domain slightly larger than the original yarn diameter was then created to enclose the filament assembly. The top and bottom edges of the rectangle were used directly as the moisture inlet (100% RH) and outlet (40% RH) boundaries, as shown in Figure 3.

The PET filaments were assigned solid properties of the yarn material (density ρ_y, thermal conductivity k_y, and heat capacity $C_{p,y}$). The surrounding domain was assigned air properties and treated as an ideal gas. The air density, thermal conductivity, and heat capacity were set to representative values at the test condition (density 1.184 $kg \cdot m^{-3}$, thermal conductivity 0.026 $W \cdot m^{-1} \cdot K^{-1}$, heat capacity 1003.62 $J \cdot kg^{-1} \cdot K^{-1}$).

For each configuration, the reported responses were calculated as the average of the 20 independent random filament layouts. The corresponding replica-to-replica variation was used to evaluate the sensitivity of the predicted transport response to random filament placement.

To determine an appropriate number of random replicas for each (dpf, Nf, φ) case, we evaluated how the estimated variability of the heat flux changes with the replica count. Figure 4 compares the distribution of the coefficient of variation (CV, %) calculated from different replica subsets. For the 5-replica sets, the CV distribution shifts across the four groups (1–5, 6–10, 11–15, and 16–20) and shows a widespread with several high-CV outliers. This indicates that using only 5 replicas can produce unstable results because the estimated variability depends strongly on which five random filament layouts are selected.

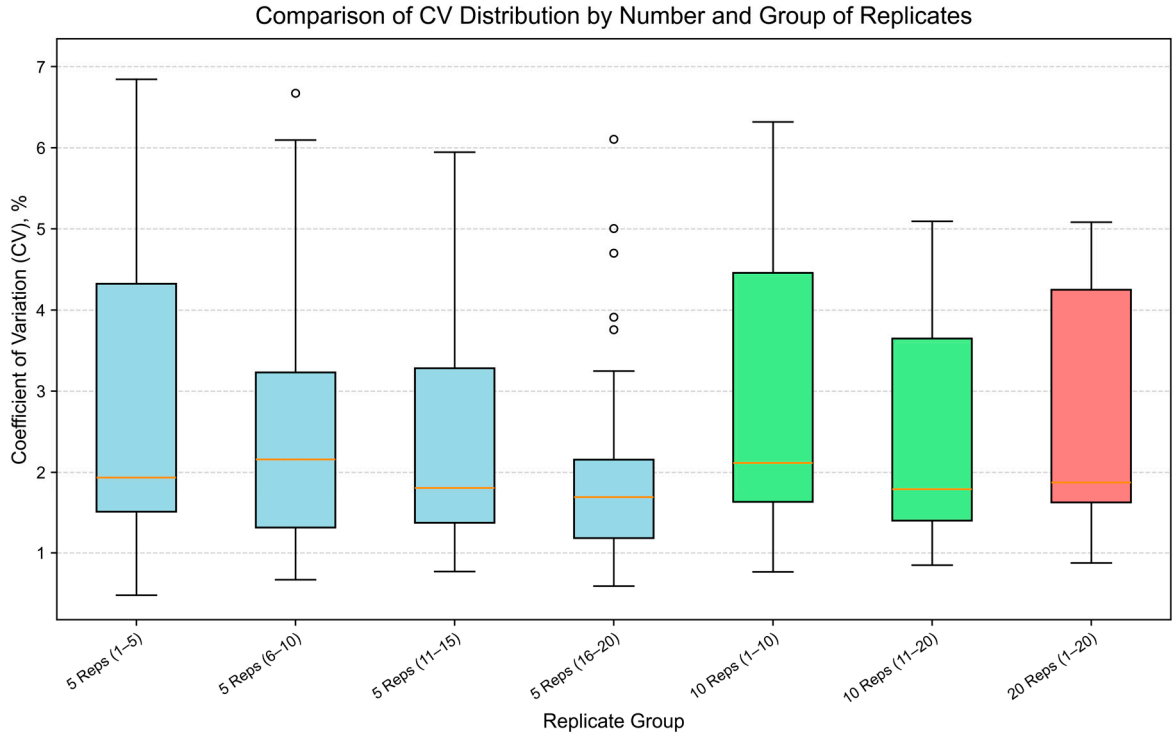


Figure 4. CV distribution of heat flux across different replicate-group selections (n = 5, 10, 20).

When the replica count is increased to 10, the CV distribution becomes narrower than in the 5-replica case, but group-to-group differences remain between replicas 1–10 and 11–20. This means that 10 replicas reduce sampling noise but still leave sensitivity to the selected subset. Using all 20 replicas provides the most consistent CV distribution, with reduced spread and less dependence on replica grouping. Therefore, each base model in this study was simulated with 20 independent random filament distributions.

2.4. FE Model Validation

For validation, the five experimental yarn-array configurations listed in Table 1 were mapped to the closest corresponding simulation inputs in the factorial design. The experimental denier per filament was calculated as the yarn linear density divided by the number of filaments. The number of filaments was directly matched to the corresponding simulation level when available, and the measured packing factor was assigned to the nearest packing-factor level used in the simulation design. The resulting mapping is summarized in Table 4. For example, the 72-filament, 150-denier yarn has an experimental dpf of 150/72 = 2.08 and was therefore mapped to the dpf = 2 simulation level. Similarly, the 72-filament, 75-denier yarn has an experimental dpf of 75/72 = 1.04 and was mapped to dpf = 1. The experimental packing factors of 0.43, 0.51, and 0.52 were mapped to the nearest simulation levels of 0.45, 0.50, and 0.50, respectively.

Table 4. Mapping between experimental validation specimens and finite element simulation inputs.

Experimental Configuration	Exact dpf	Measured φ	Twist Level	Mapped Simulation Input	Model ID
72 fil., 150 D, FDY Repreve	150/72 = 2.08	0.55	0 tpm	dpf = 2, Nf = 72, φ = 0.55	18
72 fil., 75 D, FDY Repreve	75/72 = 1.04	0.43	0 tpm	dpf = 1, Nf = 72, φ = 0.45	4
48 fil., 150 D, FDY Repreve/Ciclo	150/48 = 3.13	0.51	600 tpm	dpf = 3, Nf = 48, φ = 0.50	26
72 fil., 150 D, FDY Repreve	150/72 = 2.08	0.52	600 tpm	dpf = 2, Nf = 72, φ = 0.50	17
72 fil., 75 D, FDY Repreve	75/72 = 1.04	0.55	1200 tpm	dpf = 1, Nf = 72, φ = 0.55	6

It should be noted that the validation covers five representative configurations rather than all 36 unique factorial combinations. Therefore, the validation should be interpreted as a representative validation of the model response over a limited subset of the design space. The full-factorial simulations were subsequently used to analyze relative parameter trends within the prescribed levels of dpf, the number of filaments, and packing factor.

Figure 5 validates the numerical framework against SGHP measurements for five representative yarn configurations. Two numerical geometries are compared. The elliptical cross-section model comes from our previous study and uses measured specimen geometry. The circular cross-section model is the simplified geometry adopted in the present work for the full-factorial analysis. In both models, the same coupled heat–moisture physics and the same boundary conditions were used; the main difference is the assumed cross-sectional shape.

In Figure 5a, both models reproduce the experimental level and the case-to-case trend in heat flux. The circular model predicts heat flux values that are close to the measurements across all five configurations. The experimental data show deviations within about ±8% while the circular model is slightly lower than the experiment for four cases (by roughly 5%). The elliptical model predicts heat flux values that are generally higher than the experiment for these configurations. For most cases, the experiment falls between the circular and elliptical predictions, which shows that the cross-sectional envelope has a clear influence on the predicted evaporative heat loss.

The comparison also confirms that the simplified geometry captures the correct ordering between configurations. For example, the configuration with lower packing (Nf = 72, φ = 0.45, dpf = 1) shows the highest heat flux among the Nf = 72 cases, while the

higher-packing cases ($\varphi = 0.55$) show lower heat flux. This same pattern appears in the experimental bars and in both model predictions, indicating that the circular model captures the sensitivity of heat flux to packing factor and the number of filaments within the tested range.

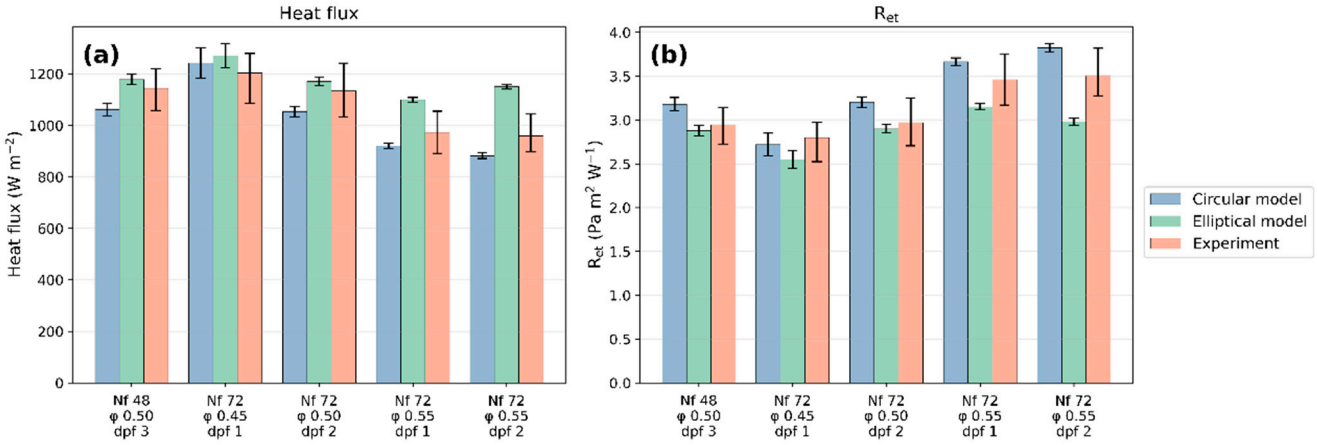


Figure 5. Validation of numerical predictions against SGHP measurements for selected yarn configurations: (**a**) heat flux and (**b**) moisture resistance R_{et}. Bars show mean values for the circular model (full-factorial geometry), the elliptical model (measured geometry), and experiment. Error bars indicate experimental scatter and the variability across random filament layouts in the simulations.

In Figure 5b, the circular model also provides good agreement for moisture resistance. The circular model predictions stay within about −3% to +9% of the experimental means for the five cases. The circular model tends to give slightly higher R_{et} than the experiment, which is consistent with its slightly lower predicted heat flux in Figure 5a. The elliptical model predicts R_{et} values that are generally lower than the experiment for these configurations. This is again consistent with the higher heat flux predicted by the elliptical geometry, since stronger vapor transport corresponds to lower resistance under the same driving conditions.

Across the five configurations, both models follow the same experimental trend in R_{et}. Cases with higher packing ($\varphi = 0.55$) show higher resistance than the lower-packing case ($\varphi = 0.45$) at the same number of filaments and dpf. This trend is present in the measurements and is reproduced by the circular model, which is important for the later factorial interpretation. The error bars for the simulations reflect variability across random filament layouts under the same (dpf, Nf, φ) conditions. In this comparison, the elliptical model shows a slightly narrower spread than the circular model. Even so, the circular model remains stable across configurations and preserves the correct ranking of responses.

Because three validation configurations were twisted yarns, the validation results should be interpreted with this geometric limitation in mind. The low coefficient of variation across the 20 random replicas indicates stable effective 2D predictions for the mapped medium- and high-packing cases, but the model does not explicitly represent helical transport pathways.

Overall, Figure 5 shows that the simplified circular cross-section model can capture both heat flux and R_{et} with good accuracy for the tested yarn configurations, while retaining the correct sensitivity to packing factor and the number of filaments. This supports the use of the circular cross-section assumption as an efficient and consistent geometric basis for the full-factorial study. Although larger-scale yarn-density variability may affect the absolute measured flux, the validation results show reasonable agreement with the experimental data for the representative yarn-array configurations. This suggests that such variability

was reduced by the controlled sample-warping procedure, although it may still contribute to experimental scatter.

3. Results and Discussion

3.1. Heat Flux and Moisture Resistance

Figure 6 summarizes the simulated heat flux for the 36 cases, with each boxplot representing the distribution across the 20 random filament distributions. Results are organized by denier per filament (dpf = 1, 2, 3) in three panels, and within each panel by the number of filaments (Nf = 48, 72, 96, 144) and packing factor (φ = 0.45, 0.50, 0.55). Two patterns are consistent across all panels. First, heat flux decreases monotonically with increasing φ. Second, for a fixed φ, heat flux generally decreases as either Nf or dpf increases.

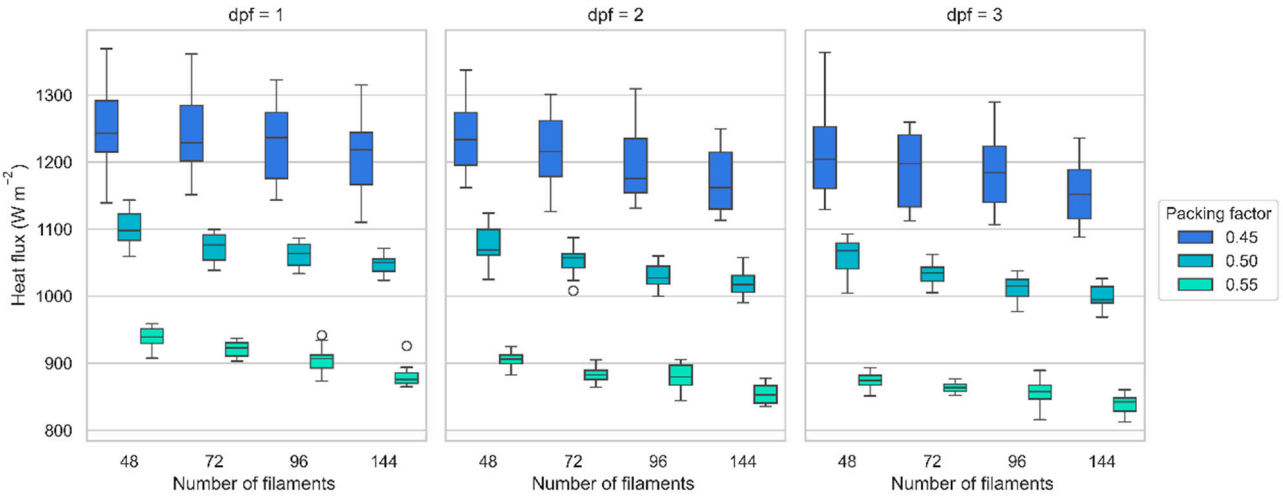


Figure 6. Effects of the number of filaments (Nf) and packing factor (φ) on heat flux across denier-per-filament levels (dpf).

It can be seen from Figure 6 that packing factor has the largest impact on heat flux. When averaged over all Nf and dpf levels, the mean heat flux drops from 1208 W·m^{-2} at φ = 0.45 to 1048 W·m^{-2} at φ = 0.50, and further to 883 W·m^{-2} at φ = 0.55. This corresponds to an overall reduction of about 27% from φ = 0.45 to φ = 0.55. The same magnitude is observed within each dpf panel (about 26–28% decrease from φ = 0.45 to φ = 0.55). This strong effect is expected because increasing φ increases the solid fraction and reduces the available void space for vapor transport. The pore network also becomes more constricted. These changes reduce the effective vapor transport capacity and therefore reduce the evaporative heat flux under the same boundary driving force. The separation between φ levels is also large compared with the within-level variation. Across the entire dataset, the mean range within a fixed φ is relatively narrow (about 1157–1253 W·m^{-2} at φ = 0.45, 999–1101 W·m^{-2} at φ = 0.50, and 840–939 W·m^{-2} at φ = 0.55). In contrast, shifting packing factor changes the mean by roughly 160–325 W·m^{-2}, depending on which levels are compared.

Number of filaments has a smaller but consistent effect. When averaged over dpf and φ, the mean heat flux decreases from 1073 W·m^{-2} at Nf = 48 to 1020 W·m^{-2} at Nf = 144, which is about a 5% reduction. Within each dpf panel, the downward trend with Nf is present for all φ levels. The Nf effect is modest because, in this design, changing Nf at fixed φ changes the yarn cross-sectional scale and the internal void geometry in a coupled way. Increasing Nf tends to increase the geometric complexity and tortuosity of the inter-filament pore network. This generally increases resistance to vapor transport and

reduces the heat flux. The magnitude depends somewhat on φ. For example, at dpf = 1, the drop from Nf = 48 to 144 is about 3.4% at $\varphi = 0.45$, but about 6.4% at $\varphi = 0.55$. This indicates that filament-count effects become more visible when the structure is already relatively compact.

Denier per filament also shows a clear but smaller influence. Averaged over Nf and φ, the mean heat flux decreases from 1072 $W \cdot m^{-2}$ (dpf = 1) to 1023 $W \cdot m^{-2}$ (dpf = 3), which is about a 4.5% reduction. This is visible in Figure 6 as a downward shift in the distributions from the dpf = 1 panel to the dpf = 3 panel. The dpf effect becomes stronger at higher packing. For a given Nf, the reduction from dpf = 1 to dpf = 3 is typically ~3–4% at φ = 0.45–0.50, but increases to ~6–7% at $\varphi = 0.55$. This interaction is physically reasonable. At higher packing, transport pathways are narrower, so changes in filament size alter the local gap distribution more strongly. In that regime, a small change in characteristic pore size can cause a larger change in effective transport.

The boxplots in Figure 6 show that random filament placement introduces measurable variability, but the magnitude depends strongly on φ. At low packing ($\varphi = 0.45$), the distributions are visibly wider, and outliers occur more often. Quantitatively, the average coefficient of variation across cases at $\varphi = 0.45$ is about 4.5%, with the largest case reaching about 5.1% (dpf = 1, Nf = 48, $\varphi = 0.45$). In contrast, at $\varphi = 0.50$ and $\varphi = 0.55$ the average CV drops to about 1.8% and 1.5%, respectively, and the narrowest case is below 1% (about 0.88% at dpf = 3, Nf = 72, $\varphi = 0.55$). This behavior indicates that geometry randomness matters most when the yarn is loosely packed. In that case, a few random changes in filament positions can noticeably change pore connectivity and local open channels. As φ increases, the structure becomes more constrained and the transport pathways become more uniform, so the heat-flux response becomes less sensitive to the specific random layout.

Overall, Figure 6 shows a clear hierarchy of effects: packing factor dominates the heat-flux response (≈27% change across its range), while Nf and dpf provide secondary shifts (≈5% and ≈4–5% on average). Random filament placement contributes additional spread, but mainly at $\varphi = 0.45$. This ranking supports using φ as the primary design lever for controlling heat flux, while Nf and dpf refine the response and influence the sensitivity to geometric randomness.

Figure 7 reports the predicted total moisture flux ($kg \cdot m^{-2} \cdot s^{-1}$) for the full-factorial design, where each boxplot summarizes the distribution across the 20 random filament layouts for a fixed (dpf, Nf, φ) combination. The four panels isolate the effect of the number of filaments (Nf = 48, 72, 96, 144). Within each panel, cases are ordered by packing factor φ (0.45, 0.50, 0.55) and then by dpf (1–3). The overall span of the mean responses is from 3.95×10^{-4} (highest packing, largest dpf, highest Nf) to 5.90×10^{-4} $kg \cdot m^{-2} \cdot s^{-1}$ (lowest packing, smallest dpf, lowest Nf), which is about a 33% difference across the explored design space. The medians shift in a consistent direction across all panels, which indicates that the factor effects are not dominated by random layout noise.

Packing factor φ is the strongest driver of total moisture flux. When averaged over all dpf and Nf levels, the mean flux decreases from 5.68×10^{-4} at $\varphi = 0.45$ to 4.92×10^{-4} at $\varphi = 0.50$ (a drop of 7.55×10^{-5}, about 13%), and then to 4.23×10^{-4} at $\varphi = 0.55$ (a further drop of 6.93×10^{-5}, about 14%). The net decrease from $\varphi = 0.45$ to 0.55 is 1.45×10^{-4}, or about 26%. This stepwise separation is visible within every Nf panel, and it is much larger than the interquartile ranges of the boxplots. The interpretation is consistent with the geometry: increasing φ reduces void fraction and constricts the connected pore space, which lowers the effective vapor transport capacity under the same boundary driving force and therefore reduces the total moisture flux.

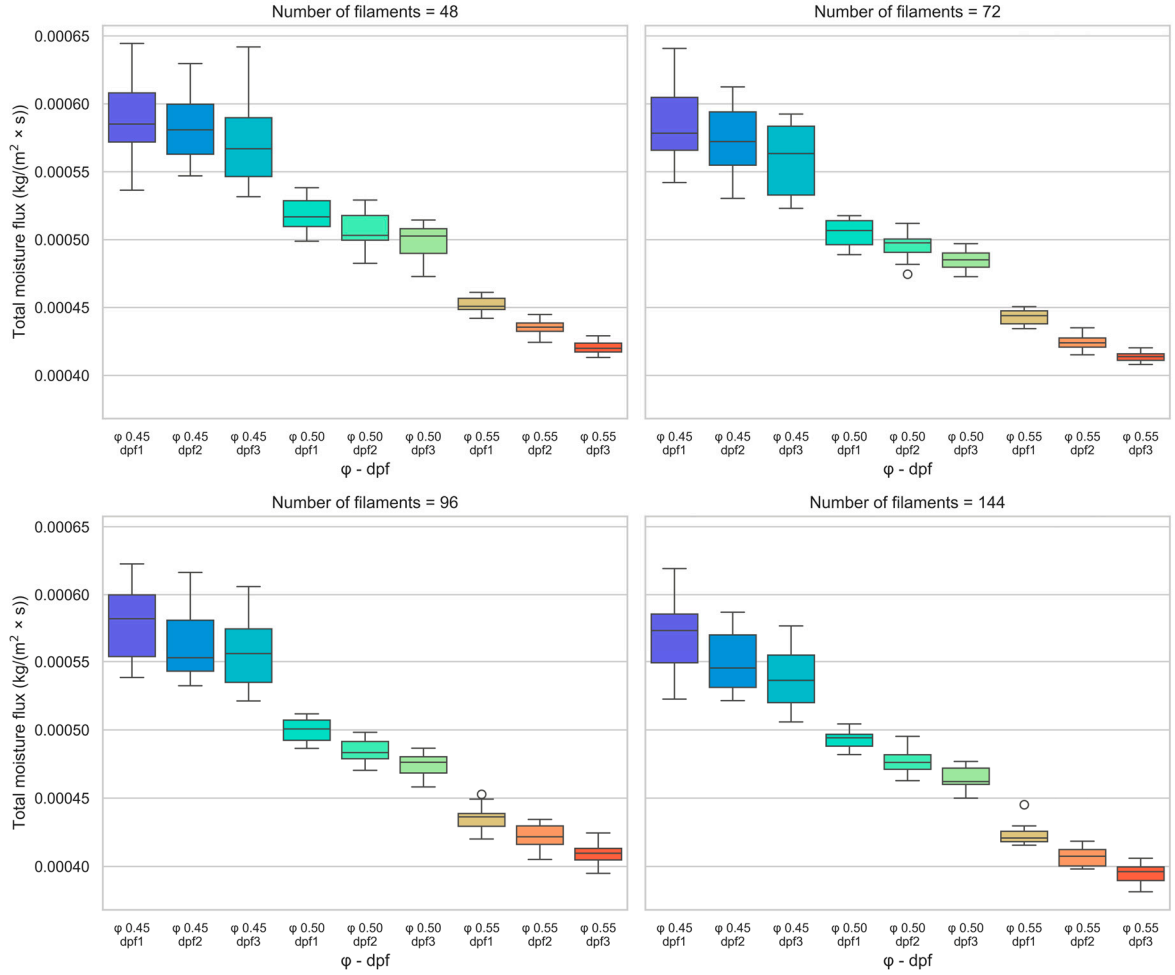


Figure 7. Total moisture flux distributions across packing factor (φ) and denier-per-filament (dpf), stratified by filament number (Nf).

Denier per filament produces a clear secondary effect. Averaged over Nf and φ, the mean flux decreases from 5.08×10^{-4} at dpf = 1 to 4.82×10^{-4} kg·m^{-2}·s^{-1} at dpf = 3, a reduction of 2.61×10^{-5} (about 5%). The dpf effect also depends on packing. At $\varphi = 0.45$, the mean decreases from 5.81×10^{-4} (dpf = 1) to 5.56×10^{-4} (dpf = 3), a change of 2.50×10^{-5} (about 4.3%). At $\varphi = 0.55$, the mean decreases from 4.38×10^{-4} to 4.10×10^{-4}, a change of 2.80×10^{-5} (about 6.4%). This stronger effect at higher φ is consistent with a pore-size argument: when the structure is already compact, changes in filament size and the resulting local gap distribution have a larger impact on the effective transport paths, so the flux becomes more sensitive to dpf.

The number of filaments Nf has a moderate but consistent influence when compared across panels. Averaged over φ and dpf, the mean flux decreases from 5.08×10^{-4} at Nf = 48 to 4.80×10^{-4} at Nf = 144, a reduction of 2.80×10^{-5} (about 5.5%). This effect appears at each packing level. For example, at $\varphi = 0.45$ the mean decreases from 5.81×10^{-4} (Nf = 48) to 5.53×10^{-4} (Nf = 144), while at $\varphi = 0.55$ it decreases from 4.36×10^{-4} to 4.08×10^{-4}. Although the absolute drop is similar, the relative drop is slightly larger at higher packing because the baseline moisture flux is lower. Mechanistically, increasing Nf increases the geometric complexity of the inter-filament pore network and increases the characteristic cross-sectional scale used in the constructed yarn boundary, which together tend to reduce net transport under the same boundary conditions.

The boxplot in Figure 7 spreads quantify the contribution of random filament placement. Variability is highest at low packing and decreases as φ increases. Using the

20-replica statistics, the average coefficient of variation across cases is 4.50% at $\varphi = 0.45$, dropping to 1.84% at $\varphi = 0.50$ and 1.45% at $\varphi = 0.55$. The largest CV occurs for the loosest, smallest-filament case (Nf = 48, $\varphi = 0.45$, dpf = 1), where CV reaches 5.08%, while the minimum CV across the design is below 1%. This pattern indicates that layout randomness matters most when the yarn is loosely packed, because small shifts in filament positions can create more open or more constricted pathways through the void space. In denser structures, filament positions are more constrained, and the pore network becomes more uniform, so replica-to-replica scatter is reduced.

Overall, Figure 7 indicates a clear hierarchy for total moisture flux: packing factor controls the dominant changes (about a 26% decrease from 0.45 to 0.55), while dpf and Nf introduce smaller but systematic decreases (each about 5% over their ranges). Random filament placement contributes additional scatter mainly at $\varphi = 0.45$, but it does not obscure the main factor trends or change their ordering.

3.2. Analysis of Variance

A three-way analysis of variance (ANOVA) was conducted on the steady state response (mean heat flux) using an ordinary least squares full-factorial model comprising the three categorical factors: the number of filaments, packing factor and denier per filament, plus all two and three way interaction terms. The ANOVA result is summarized in Table 5.

Table 5. Variance decomposition and effect size of heat flux (Type II ANOVA).

Source	df	SS	SS (% Total)	F	*p*-Value	Partial η^2
φ	2	1.643×10^7	92.354	6985.288	0	0.9533
dpf	2	2.752×10^5	1.547	117.018	1.955×10^{-44}	0.2549
Nf	3	2.647×10^5	1.488	75.013	5.927×10^{-42}	0.2476
Nf $\times$ φ	6	6.920×10^3	0.0389	0.981	4.372×10^{-1}	0.00853
Nf $\times$ dpf	6	1.174×10^3	0.00660	0.166	9.856×10^{-1}	0.00146
φ $\times$ dpf	4	5.680×10^2	0.00319	0.121	9.751×10^{-1}	0.000706
Nf $\times$ φ $\times$ dpf	12	7.209×10^3	0.0405	0.511	9.085×10^{-1}	0.00888
Residual	684	8.044×10^5	4.522	—	—	—

Table 5 confirms, in a statistical sense, the trends already visible in the heat-flux boxplots. The total sum of squares is 1.779×10^7, and the packing factor φ accounts for 92.35% of this variance (Sum of squares (SS) $= 1.643 \times 10^7$). The corresponding effect size is very large (partial $\eta^2 = 0.953$), and the F statistic is extremely high (F value = 6985.3; the *p*-value is reported as 0, i.e., vanishingly small). In contrast, denier per filament dpf and the number of filaments Nf each explain only a small fraction of the variance, 1.55% and 1.49%, respectively, although both are still statistically significant ($p \sim 10^{-44}$ for dpf and $p \sim 10^{-42}$ for Nf). All interaction terms are negligible in magnitude: the combined interaction contribution is only 0.089% of the total SS, and none of the interaction F-tests are significant (all $p \geq 0.44$). The residual accounts for 4.52% of the variance, which is consistent with the replica-to-replica scatter introduced by random filament placement and any remaining numerical dispersion. Overall, Table 5 supports a clear hierarchy of effects for heat flux: φ dominates, while dpf and Nf act as secondary modifiers, and interaction effects are not needed to explain the response over the tested design space.

Table 6 provides a practical interpretation of these results using the GLM main-effects estimates relative to the baseline configuration (Nf = 48, $\varphi = 0.45$, dpf = 1), which has a predicted heat flux of 1253.2 W·m^{-2}. Increasing packing from $\varphi = 0.45$ to 0.50 reduces heat flux by 152.2 W·m^{-2} (-12.14%, $p = 1.73 \times 10^{-39}$), and increasing to 0.55 reduces it by 360.8 W·m^{-2} (-28.79%, $p = 4.35 \times 10^{-145}$). These shifts are an order of magnitude

larger than the changes associated with dpf or Nf, which is consistent with the variance decomposition. For dpf, moving from dpf = 1 to 2 changes heat flux by only -16.1 W·m^{-2} (-1.29%) and is not significant ($p = 0.137$), whereas dpf = 3 produces a larger reduction of -41.9 W·m^{-2} (-3.34%, $p = 1.23 \times 10^{-4}$). For the number of filaments, Nf = 72 is not distinguishable from the baseline (-11.0 W·m^{-2}, -0.88%, $p = 0.309$), while Nf = 96 and Nf = 144 produce small but significant decreases of -25.6 W·m^{-2} (-2.04%, $p = 0.0186$) and -42.2 W·m^{-2} (-3.36%, $p = 1.11 \times 10^{-4}$), respectively. Taken together, Tables 5 and 6 show that the heat-flux response is primarily controlled by packing factor through its impact on void fraction and pathway constriction, while changes in filament size and filament count provide smaller, systematic adjustments. The lack of significant interactions indicates that, within this parameter range, the heat-flux response can be described accurately using main effects, which simplifies interpretation and supports the factorial analysis framework used in this study.

Table 6. Baseline and marginal effects on predicted heat flux.

Factor	Level (vs. Baseline)	Predicted Heat Flux (Baseline Others)	Δ Heat Flux vs. Baseline	Δ% vs. Baseline	*p*-Value
Baseline	Nf = 48, φ = 0.45, dpf = 1	1253.195	0	0	—
φ	0.50	1101.040	−152.155	−12.14%	1.73×10^{-39}
φ	0.55	892.421	−360.775	−28.79%	4.35×10^{-145}
dpf	2	1237.050	−16.145	−1.29%	0.137 (ns)
dpf	3	1211.305	−41.890	−3.34%	1.23×10^{-4}
Nf	72	1242.165	−11.030	−0.88%	0.309 (ns)
Nf	96	1227.620	−25.575	−2.04%	0.0186
Nf	144	1211.030	−42.165	−3.36%	1.11×10^{-4}

Note: ns, not statistically significant ($p \geq 0.05$).

For the total moisture flux response, Table 7 shows the same overall structure as the heat-flux ANOVA, but with a slightly smaller dominance of packing. Packing factor explains 88.14% of the total variance (F = 4794.8, *p*-value effectively zero as reported), with a very large effect size (partial $\eta^2 = 0.933$). Denier per filament and number of filament are secondary contributors and are comparable in magnitude: 2.74% for dpf (F = 149.0, $p = 1.99 \times 10^{-54}$, partial $\eta^2 = 0.303$) and 2.70% for Nf (F = 97.8, $p = 1.08 \times 10^{-52}$, partial $\eta^2 = 0.300$). All interaction terms are negligible in variance contribution (each $\leq 0.05\%$ of total SS) and are not significant (e.g., $p = 0.612$ for Nf × φ; $p = 0.948$ for Nf × φ × dpf). The residual is 6.29%, which is slightly larger than in the heat-flux ANOVA and is consistent with the remaining replica-to-replica variability from random filament placements.

Table 7. Variance decomposition and effect size of total moisture flux (Type II ANOVA).

Source	df	Sum of Squares (SS)	SS (% Total)	F	*p*-Value	Partial η^2
φ	2	2.5126×10^{-3}	88.14	4794.81	0	0.933
dpf	2	7.8059×10^{-8}	2.74	148.96	1.991×10^{-54}	0.303
Nf	3	7.6891×10^{-8}	2.70	97.82	1.084×10^{-52}	0.300
Nf × φ	6	1.1737×10^{-9}	0.04	0.75	6.123×10^{-1}	0.007
Nf × dpf	6	6.8447×10^{-10}	0.02	0.44	8.554×10^{-1}	0.004
φ × dpf	4	5.8335×10^{-10}	0.02	0.56	6.943×10^{-1}	0.003
Nf × φ × dpf	12	1.3796×10^{-9}	0.05	0.44	9.478×10^{-1}	0.008
Residual	684	1.7922×10^{-7}	6.29			

Table 8 translates the ANOVA ranking into practical marginal changes using the main-effects GLM relative to the baseline (Nf = 48, φ = 0.45, dpf = 1), for which the

predicted moisture flux is 5.90×10^{-4} kg·m^{-2}·s^{-1}. Increasing packing reduces moisture flux strongly: moving to $\varphi = 0.50$ decreases total moisture flux by 7.2×10^{-5} (-12.14%, $p = 2.67 \times 10^{-39}$), and moving to $\varphi = 0.55$ decreases total moisture flux by 1.38×10^{-4} (-23.37%, $p = 1.83 \times 10^{-109}$). The dpf effect is smaller: dpf = 2 changes total moisture flux by only -1.26% and is not significant ($p = 0.146$), while dpf = 3 decreases total moisture flux by 2.0×10^{-5} (-3.32%, $p = 1.40 \times 10^{-4}$). The Nf effect is also modest: Nf = 72 is not distinguishable from baseline (-0.87%, $p = 0.319$), whereas Nf = 96 (-2.01%, $p = 0.0206$) and Nf = 144 (-3.37%, $p = 1.14 \times 10^{-4}$) show small but significant reductions.

Table 8. Baseline and marginal effects on predicted moisture flux.

Factor	Level (vs. Baseline)	Predicted Moisture Flux	Δ Moisture Flux vs. Baseline	Δ% vs. Baseline	*p*-Value
Baseline	Nf = 48, φ = 0.45, dpf = 1	5.89866×10^{-4}	0	0.00%	—
φ	0.5	5.1824×10^{-4}	-7.1616×10^{-5}	−12.14%	2.673×10^{-39}
φ	0.55	4.5201×10^{-4}	-1.3785×10^{-4}	−23.37%	1.833×10^{-109}
dpf	2	5.8241×10^{-4}	-7.4500×10^{-6}	−1.26%	1.460×10^{-1}
dpf	3	5.7025 × 10-4	-1.9606×10^{-5}	−3.32%	1.398×10^{-4}
Nf	72	5.8475×10^{-4}	-5.1055×10^{-6}	−0.87%	3.189×10^{-1}
Nf	96	5.7797×10^{-4}	-1.1883×10^{-5}	−2.01%	2.055×10^{-2}
Nf	144	5.6999×10^{-4}	-1.9868×10^{-5}	−3.37%	1.139×10^{-4}

Taken together, the heat-flux and moisture-flux ANOVA results support the same hierarchy of effects across the full-factorial space. In both cases, packing factor is the dominant control variable, while dpf and Nf provide smaller, systematic shifts, and interactions are negligible within the studied ranges. This justifies interpreting both responses primarily through main effects, and it supports the use of the simplified factorial framework to link microstructure (especially packing factor) to coupled heat–moisture transport performance.

3.3. Velocity Fields Distribution

Figure 8 shows the instantaneous flow fields at t = 0.1 s for selected cross-sections. The colored background indicates the local velocity magnitude in the air-filled pore domain, while the arrows represent the in-plane velocity vectors. Therefore, the key information in this figure is how the pore geometry controls flow penetration and bypass, under otherwise identical thermal conditions.

A clear transition is observed as φ increases, and the pattern is consistent for all number of filaments shown. At $\varphi = 0.45$, strong velocity vectors appear not only in the lateral gaps outside the filament cluster, but also within the inter-filament voids. In several cases, the arrows form connected paths that penetrate into the yarn interior, indicating that the pore network remains sufficiently open to support internal flow rather than forcing the gas to bypass around the fiber bundle. This means a larger portion of the cross-section actively participates in transport, because the flow can access internal voids and exchange across a wider area. Along each column, increasing Nf (48 → 144) tends to make these interior paths less continuous and shifts a larger fraction of the motion toward the perimeter gaps, consistent with a more tortuous and compartmentalized pore network at higher number of filaments.

At $\varphi = 0.50$, the internal velocity field becomes weaker and more fragmented as shown in Figure 8. High velocities are still visible near the side gaps, but inside the filament assembly the arrows are shorter and less continuous, suggesting partial blockage of through-paths and more localized motion. The effect of Nf is clearer at this intermediate packing: cases with higher Nf show less interior penetration and a stronger preference for bypass flow near the outer gaps, whereas lower-Nf cases retain occasional interior channels. At

φ = 0.55, internal flow is largely suppressed. The velocity vectors are concentrated almost entirely near a small region along the outer gap, while the interior shows sparse and weak arrows, implying that the compact pore structure is poorly connected for flow penetration. Under this compact state, the visual differences among Nf levels become subtle because the dominant transport pathway is already restricted to the perimeter bypass region.

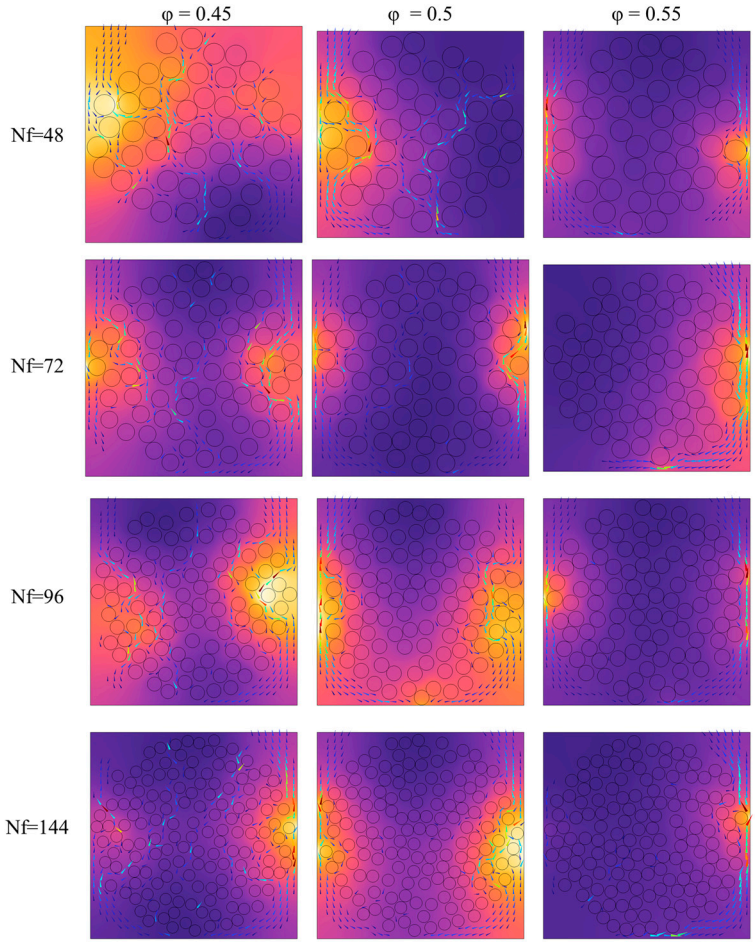


Figure 8. Field distribution and streamline patterns in yarn cross-sections for varying filament number and packing factor (φ). Columns correspond to φ = 0.45, 0.50, and 0.55, and rows correspond to Nf = 48, 72, 96, and 144. The colored background indicates the velocity magnitude field, where warmer colors mark regions of stronger flow. Arrows represent local flow velocity vectors (direction and relative magnitude), and streamlines depict the flow paths.

These flow-field observations provide a mechanistic explanation for the macroscopic trends reported earlier. The progressive loss of internal flow from φ = 0.45 to 0.55 is consistent with the strong reduction in heat/moisture flux and the increase in R_{et}, and it explains why the packing factor dominates the ANOVA results compared with dpf and Nf. At a fixed packing factor, the systematic (but smaller) reduction in interior penetration with increasing Nf provides a physical basis for the secondary main effect of Nf observed in the ANOVA, while the weak interaction terms are consistent with the fact that Nf mainly tunes pathway continuity rather than changing the transport regime set by packing factor.

Figure 9 shows instantaneous fields at t = 0.1 s for a fixed packing factor φ = 0.50. This figure is used to isolate the roles of dpf and Nf under an intermediate packing state. We focus on φ= 0.50 because at φ = 0.55 the structure is so compact that internal flow is weak for most cases, and the differences among dpf and Nf become difficult to distinguish in the velocity field plots.

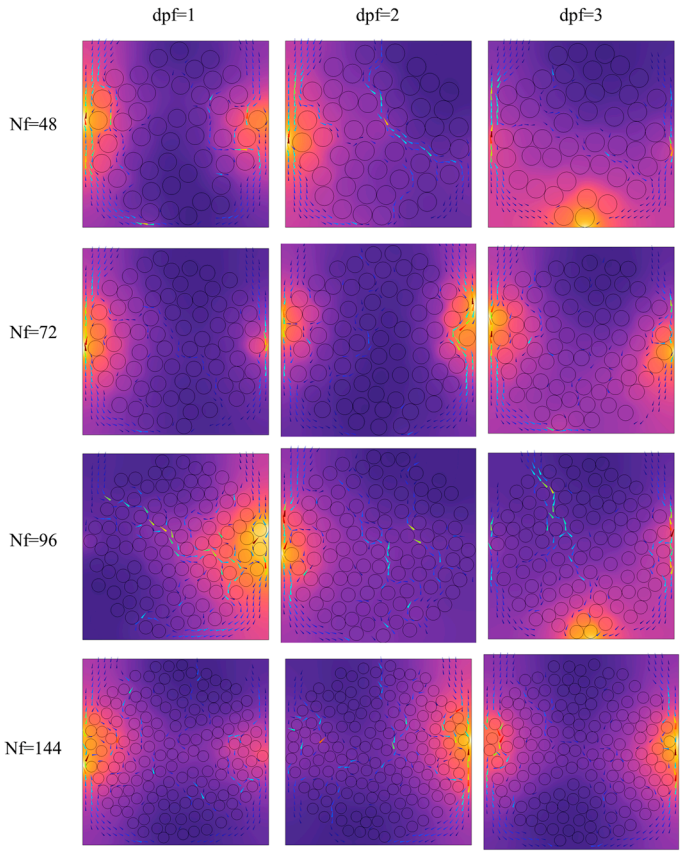


Figure 9. Field distribution and streamline patterns in yarn cross-sections for varying filament number and denier per filament (dpf). Columns correspond to dpf = 1, 2, and 3, and rows correspond to Nf = 48, 72, 96, and 144. The colored background indicates the air-flow field, where warmer colors mark regions of stronger flow. Arrows represent local flow velocity vectors, and streamlines depict the flow paths.

At $\varphi = 0.50$, the flow is dominated by bypass regions near the lateral gaps, but partial penetration into the filament assembly is still possible in some cases. The extent of this penetration decreases as either dpf or Nf increases. At Nf = 48, the dpf = 1 case shows the most visible internal motion, with vectors extending beyond the perimeter region and forming at least one connected path into the interior. As dpf increases from 1 to 3 at the same Nf, the internal vectors become shorter and more fragmented, and the higher-velocity zones concentrate more strongly near the side gaps. This indicates that larger filament diameter reduces the size and connectivity of the inter-filament voids, which raises the hydraulic resistance for through-bundle flow. In the macroscopic results, the same change appears as a modest but systematic reduction in heat/moisture flux and an increase in R_{et} with increasing dpf at a fixed packing factor.

A similar trend is seen when moving down each column (fixed dpf, increasing Nf from 48 to 144). At dpf = 1, the Nf = 48 and Nf = 72 cases still show some internal pathways, whereas the Nf = 144 case exhibits a flow field that is more confined to the perimeter, with weaker vectors inside the filament assembly. Increasing Nf increases the number of solid obstacles and subdivides the void space into smaller pores. Even when the global packing factor is held constant, the pore network becomes more tortuous and contains more dead-end regions, so long connected channels through the interior are less likely. This explains why the Nf effect is statistically significant but smaller than the effect of packing factor: it changes connectivity and tortuosity within a given packing level rather than producing the strong step change associated with packing.

This field-level interpretation is consistent with the ANOVA and boxplot trends. At $\varphi = 0.50$, packing already sets the overall transport level, while dpf and Nf provide secondary shifts by controlling whether a limited number of internal pathways remain open. In other words, their influence at $\varphi = 0.50$ is expressed mainly through the availability and continuity of internal flow channels, not through a uniform scaling of velocity everywhere. This is also why their visual contrast is much weaker at $\varphi = 0.55$: once the structure becomes highly compact, most internal pathways are suppressed, and further changes in dpf or Nf mainly produce small adjustments rather than distinct flow patterns.

Figure 10 compares instantaneous fields at t = 0.1 s for a fixed number of filament Nf = 72. Cases are arranged by packing factor φ (columns: 0.45, 0.50, 0.55) and denier per filament (rows: dpf = 1, 2, 3). With Nf held constant, the figure highlights how φ and dpf reshape pore connectivity and determine whether flow can penetrate the bundle or mainly bypass it along the outer gaps.

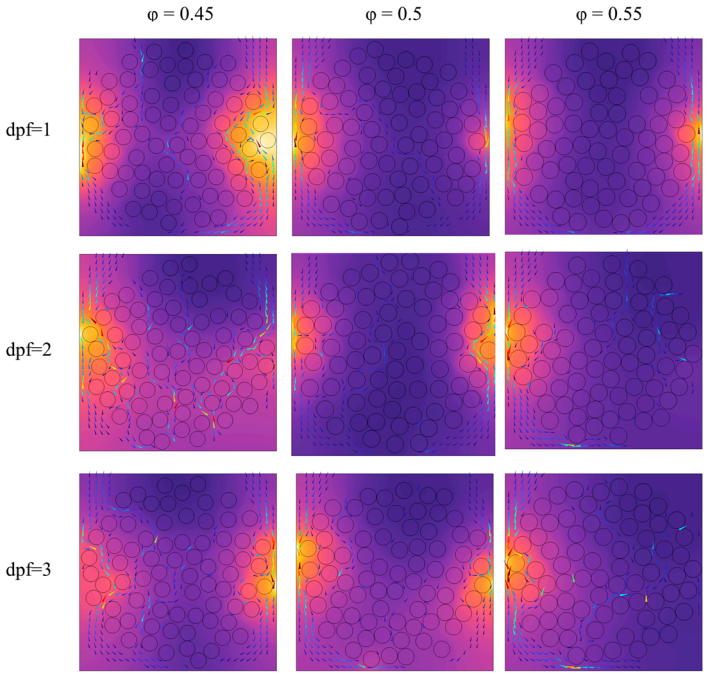


Figure 10. Field distribution and streamline patterns in yarn cross-sections for varying packing factor and denier per filament at a fixed filament number. Columns correspond to φ = 0.45, 0.50, and 0.55, and rows correspond to dpf = 1, 2, and 3. The colored background indicates the velocity magnitude field, where warmer colors mark regions of stronger flow. Arrows represent local flow velocity vectors (direction and relative magnitude), and streamlines depict the flow paths.

Packing factor controls the main transition. At $\varphi = 0.45$, the velocity field is relatively strong and not confined to the perimeter. In addition to the lateral gaps, multiple vector segments appear inside the filament assembly and extend toward the interior. This indicates that the inter-filament voids remain open and connected enough to allow partial penetration, so transport is not limited to a thin near-surface region. At this low packing, the influence of dpf on the instantaneous flow field is not visually distinct and is largely within the replica-to-replica variability caused by random filament layout. This observation is consistent with the macroscopic responses: $\varphi = 0.45$ gives higher heat and moisture flux and lower R_{et}, and it also shows larger replica-to-replica scatter because internal channels depend on the random layout.

At $\varphi = 0.50$, internal motion becomes weaker and less continuous. High velocities remain near the side gaps, but vectors inside the bundle break into short, fragmented segments. The interior is more isolated from the bypass flow, matching the intermediate

response levels (reduced flux and increased R_{et} relative to $\varphi = 0.45$). The dpf-dependence is most apparent at this intermediate packing, although the contrast remains modest: dpf = 1 may retain occasional interior paths, whereas higher dpf cases tend to be more perimeter-dominated. This is also the packing range where dpf differences are most visible, because some internal pathways still exist and can be restricted by changes in filament size.

At $\varphi = 0.55$, penetration is largely suppressed across all dpf levels. The velocity field is concentrated near narrow outer-gap regions, while the interior shows sparse, weak arrows, indicating poor through-bundle connectivity. Under these conditions, dpf mainly produces small adjustments because the dominant pathways are already constrained, which agrees with the reduced variability and weaker visual separation among dpf levels at high packing.

Figure 10 supports the hierarchy observed in the statistical analysis. Packing factor sets the transport regime by controlling whether internal penetration is possible, while dpf plays a secondary role. The effect of dpf on the flow field is subtle, where partial penetration still occurs. This is consistent with ANOVA results in which packing factor dominates heat and moisture flux and R_{et}, whereas dpf contributes a smaller but systematic shift, most evident at $\varphi \approx 0.50$.

Figure 11 summarizes the y-direction velocity (m/s) across the full-factorial space, using boxplots over the 20 random filament layouts for each (dpf, Nf, φ) case. The three panels isolate packing factor φ (0.45, 0.50, 0.55). Within each panel, velocity decreases systematically with both dpf and Nf, but the separation between φ levels is the most pronounced. When averaged over all dpf and Nf levels, the mean y-velocity drops from 0.01983 m/s at $\varphi = 0.45$ to 0.01815 m/s at $\varphi = 0.50$ (-8.5%), and to 0.01609 m/s at $\varphi = 0.55$ (a further -11.3%). Overall, increasing packing factor from 0.45 to 0.55 reduces the mean y-velocity by about 19%. This matches the field snapshots shown earlier: at low φ the pore network supports more through-bundle penetration and stronger internal motion, while at high packing factor the flow is confined mainly to narrow bypass regions near the outer gaps.

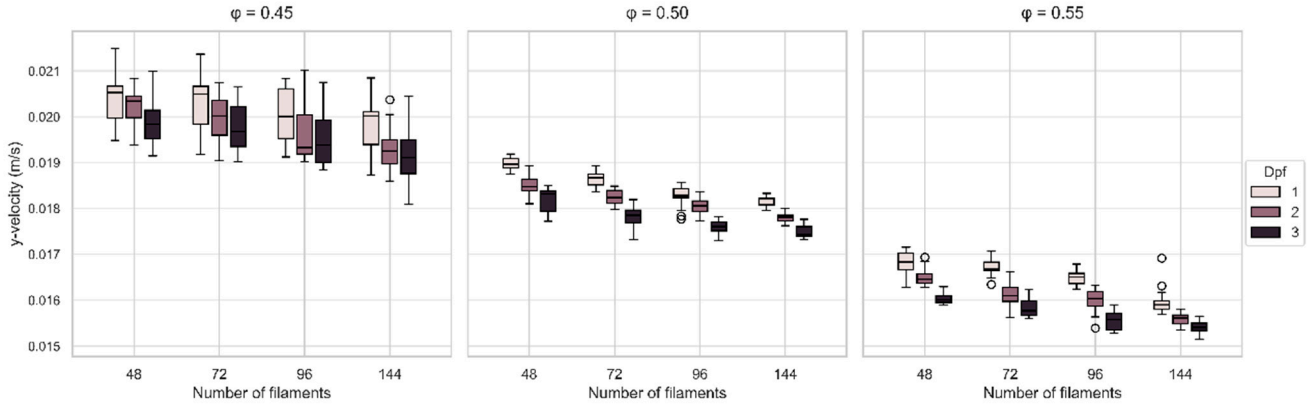


Figure 11. Y-direction air velocity as a function of filament number and denier-per-filament (dpf), stratified by packing factor (φ).

At a fixed φ, both dpf and Nf produce smaller, consistent reductions. Pooled across φ and Nf, the mean decreases from 0.01838 m/s (dpf = 1) to 0.01769 m/s (dpf = 3), a reduction of about 3.8%. Similarly, pooled across φ and dpf, increasing Nf from 48 to 144 reduces the mean from 0.01839 m/s to 0.01763 m/s (about 4.2%). Importantly, the direction is stable in every φ panel: for any given Nf, higher dpf gives lower y-velocity; for any given dpf, higher Nf gives lower y-velocity. This is consistent with the interpretation from the $\varphi = 0.50$ field comparison: increasing dpf (larger filaments) and increasing Nf (more obstacles and higher

tortuosity at the same packing factor) both reduce the continuity of internal pathways and shift the flow toward perimeter bypass, so the net y-directed motion weakens.

The box widths quantify replica-to-replica variability from random filament placement. The spread is clearly largest at $\varphi = 0.45$, where the average CV is about 2.6%, compared with ~0.94% at $\varphi = 0.50$ and ~1.19% at $\varphi = 0.55$. In absolute terms the variability is much smaller at $\varphi \geq 0.50$ than at $\varphi = 0.45$, indicating that once packing is moderate-to-high the velocity field becomes less sensitive to the specific random layout.

Overall, Figure 11 provides a flow-based link to the earlier transport results and ANOVA conclusions. The strong packing factor-dependence of y-velocity supports why φ dominates both heat flux and moisture flux, and why R_{et} increases with packing factor. The weaker but consistent effects of dpf and Nf on y-velocity match their secondary contributions in the response statistics: they tune transport mainly by adjusting pore connectivity and bypass/penetration balance within a given packing factor, rather than changing the transport regime set by packing factor.

4. Conclusions

Building on our earlier geometry-resolved work, this study adopted a simplified circular cross-section model to examine the effects of yarn microstructural parameters on isothermal water-vapor transport under ISO 11092 skin model boundary conditions. A full-factorial design was used to quantify the roles of denier per filament, the number of filaments, and packing factor. For every factor combination, twenty independent random filament layouts were generated to represent the stochastic nature (due to filament migration of twisted yarns) of filament placement and to obtain stable estimates of both the mean response and the replica-to-replica variability. A subset of cases was compared with experimental measurements and with predictions from the prior elliptical-geometry model, and the agreement confirmed that the circular cross-section assumption can accurately predict the key transport responses with good accuracy while enabling a consistent and efficient parameter study.

The full-factorial results showed a clear hierarchy of the effects. Packing factor is the dominant control variable: increasing φ consistently reduced heat flux and total moisture flux and increased moisture resistance R_{et}. Denier per filament and the number of filaments introduced smaller but systematic shifts, mainly by changing pore connectivity and tortuosity within a given packing state. The twenty-replica sampling further revealed when randomness matters. At low packing factor, internal channels may form depending on the filament layout, leading to larger scatter. At higher packing factor, flow penetration is suppressed, and transport becomes more perimeter-dominated, so variability decreases and the response becomes more repeatable. These observations were verified statistically by ANOVA. For both heat flux and moisture flux, main effects explained almost all variance, while interaction terms were negligible within the explored ranges. Field visualizations of the velocity confirmed the same mechanism and linked it directly to the response trends: low packing factor permits partial penetration through the filament assembly, whereas high packing factor forces bypass flow along narrow outer gaps. Together, the factorial design, stochastic replica sampling, and ANOVA provide a practical framework that connects controllable yarn parameters to measurable performance metrics. This framework can support yarn design and screening for thermal comfort and moisture management by identifying the most effective parameter to tune (packing factor) and the secondary parameters (dpf and Nf) that refine performance once packing is set. Furthermore, accurate yarn model would allow modeling yarn-based fabric structures such as knits and wovens.

The main physical exclusions of the model, including negligible PET sorption, no condensation, and no explicitly resolved external mass-transfer boundary layer, have

been stated in Section 2.3. Future work can extend the framework by incorporating material-specific sorption isotherms, interfacial phase change, and three-dimensional helical yarn geometry.

Author Contributions: Conceptualization, A.-F.S.; methodology, W.X., Y.Y. and A.-F.S.; software, W.X. and A.-F.S.; validation, W.X.; formal analysis, W.X.; investigation, W.X. and Y.Y.; resources, A.-F.S.; data curation, W.X. and Y.Y.; writing—original draft preparation, W.X.; writing—review and editing, A.-F.S.; visualization, W.X.; supervision, A.-F.S. and Y.Y.; project administration, A.-F.S. and Y.Y. All authors have read and agreed to the published version of the manuscript.

Funding: This research received no external funding.

Data Availability Statement: The raw data supporting the conclusions of this article will be made available by the authors on request.

Acknowledgments: During the preparation of this manuscript, the authors used Claude Code version 3.5 for assistance in generating scripts to automate the construction of finite element models in COMSOL Multiphysics. Grammarly was also used to check grammar, spelling, and punctuation. The authors reviewed and edited all tool-assisted outputs and take full responsibility for the content of this publication.

Conflicts of Interest: The authors declare no conflicts of interest.

Abbreviations

The following abbreviations are used in this manuscript:

FE	Finite element
FDY	Fully drawn yarn
Nf	Number of filaments
φ	Yarn packing factor
dpf	Denier per filament
SGHP	Sweating guarded hot plate
R_{et}	Moisture resistance
RH	Relative humidity
SS	Sum of squares
F	F-statistic
df	Degrees of freedom

References

1. Atasağun, H.G.; Okur, A.; Psikuta, A.; Rossi, R.M.; Annaheim, S. The effect of garment combinations on thermal comfort of office clothing. *Text. Res. J.* **2019**, *89*, 4425–4437. [CrossRef]
2. Černý, R.; Rovnaníková, P. Models of heat, moisture and chemical compounds transport in porous materials. In *Transport Processes in Concrete*; Černý, R., Rovnaníková, P., Eds.; Routledge: Oxfordshire, UK, 2002; pp. 155–262.
3. Henry, P.S. The diffusion of moisture and heat through textiles. *Discuss. Faraday Soc.* **1948**, *3*, 243–257. [CrossRef]
4. Zhu, Q.Y.; Xie, M.H.; Yang, J.; Li, Y. A fractal model for the coupled heat and mass transfer in porous fibrous media. *Int. J. Heat Mass Transf.* **2011**, *54*, 1400–1409. [CrossRef]
5. Xu, D.H.; Meibao, B.G.; Zhang, H.L. Numerical solution of a dynamic model of heat and moisture transfer in porous fabric under low temperature. *Int. J. Heat Mass Transf.* **2013**, *61*, 149–157. [CrossRef]
6. Fontana, É.; Donca, R.; Mancusi, E.; Ulson de Souza, A.A.; Guelli Ulson de Souza, S.M. Mathematical modeling and numerical simulation of heat and moisture transfer in a porous textile medium. *J. Text. Inst.* **2016**, *107*, 672–682.
7. Yang, Y.; Wang, X.; Liu, Z.; Zheng, C.; Lou, L.; Liu, X.; Zhang, P. Heat and moisture transfer in fabric consisting of fibers with low hygroscopicity. *Text. Res. J.* **2022**, *92*, 4764–4777. [CrossRef]
8. Zhang, J.; Liu, X.; Xie, C. Simulation analysis of the effect of fabric structural parameters on heat transfer performance. *J. Silk* **2020**, *57*, 13–18.
9. Codau, E.; Codau, T.C.; Lupu, I.G.; Raru, A.; Farima, D. Heat transfer simulation through textile porous media. *J. Text. Inst.* **2023**, *114*, 257–264.

10. Lu, X.; Meng, J.; Chen, G.; Lu, Y. Numerical simulation of heat and moisture transfer in protective clothing under high pressure steam exposure: Effect of fabric properties and steam conditions. *Int. J. Therm. Sci.* **2023**, *194*, 108550. [CrossRef]
11. Puszkarz, A.K.; Korycki, R.; Krucinska, I. Simulations of heat transport phenomena in a three-dimensional model of knitted fabric. *Autex Res. J.* **2016**, *16*, 128–137. [CrossRef]
12. Siddiqui, M.O.; Sun, D. Thermal analysis of conventional and performance plain woven fabrics by finite element method. *J. Ind. Text.* **2018**, *48*, 685–712.
13. Zheng, Z.; Zhang, N.; Zhao, X. Simulation of heat transfer through woven fabrics based on the fabric geometry model. *Therm. Sci.* **2018**, *22*, 2815–2825. [CrossRef]
14. Shen, H.; Xie, K.; Shi, H.; Yan, X.; Tu, L.; Xu, Y.; Wang, J. Analysis of heat transfer characteristics in textiles and factors affecting thermal properties by modeling. *Text. Res. J.* **2019**, *89*, 4681–4690. [CrossRef]
15. Zheng, H.; Zhou, C.; Yuan, Y. Meso-scale finite element modeling of moisture diffusion in 3D braided composite. *Int. J. Heat Mass Transf.* **2019**, *129*, 862–872. [CrossRef]
16. Yang, E.; Chu, X.; Qiu, H. Finite element simulation of thermal conductivity of weft knitted fabrics. *J. Silk* **2020**, *57*, 31–36.
17. Gu, H.; Gao, L.; Li, G.; Li, N.; Xiong, J. Simulation of coupled transient heat and water vapor transfer in porous fiber membrane with different fiber orientations and porosity. *J. Ind. Text.* **2022**, *51*, 7860S–8783S.
18. Lolaki, A.; Shanbeh, M.; Borhani, S. Effect of structural parameters of porous yarns and fabric on air permeability and moisture transfer of double-face woven fabrics. *J. Text. Inst.* **2017**, *108*, 992–1000.
19. Li, X.; Xu, Y.; Huang, X. Numerical analysis of the influence of macropore on thermal conductivity of porous media. *J. North China Electr. Power Univ. Nat. Sci. Ed.* **2012**, *39*, 76–79.
20. Xie, L.; Cong, S.; Xie, Q. Simulation research and development trend of heat and moisture coupling of porous fabrics. *J. Silk* **2014**, *51*, 41–47.
21. Cai, Y.; Yang, Y.; Qian, J. Conductivity of woven fabrics based on structural parameters. *Adv. Text. Tech.* **2021**, *29*, 43–49. [CrossRef]
22. Yang, Y.; Wang, H.; Yan, H.; Ni, Y.; Li, J. Modeling and influence on effective thermal conductivity of woven fabrics based on structure parameters. *Int. J. Cloth. Sci. Technol.* **2023**, *35*, 938–951. [CrossRef]
23. Siddiqui, M.O.; Farooq, S.; Husain, M.D.; Faisal, S. Prediction of air permeability and effective thermal conductivity of multifilament polyester yarn by finite element analysis. *Polimery* **2023**, *68*, 6–18. [CrossRef]
24. Wang, H.; Li, J.; Liu, Z.; Yang, Y.; Seyam, A.F. Three-dimensional simulation of heat and moisture transfer in woven fabric structures. *Text. Res. J.* **2024**, *94*, 2232–2252. [CrossRef]
25. Özdil, N.; Marmaralı, A.; Kretzschmar, S.D. Effect of yarn properties on thermal comfort of knitted fabrics. *Int. J. Therm. Sci.* **2007**, *46*, 1318–1322. [CrossRef]
26. Čubrić, I.S.; Skenderi, Z.; Mihelić-Bogdanić, A.; Andrassy, M. Experimental study of thermal resistance of knitted fabrics. *Exp. Therm. Fluid Sci.* **2012**, *38*, 223–228. [CrossRef]
27. Lee, S.; Obendorf, S.K. Statistical modeling of water vapor transport through woven fabrics. *Text. Res. J.* **2012**, *82*, 211–219. [CrossRef]
28. Matusiak, M.; Kamińska, D. Liquid moisture transport in cotton woven fabrics with different weft yarns. *Materials* **2022**, *15*, 6489. [CrossRef] [PubMed]
29. Lu, Y.; Hong, Q.; Sun, F.; Gao, W.; Xu, C. Effect of yarn structure on the liquid moisture transport in yarns. *J. Text. Inst.* **2022**, *113*, 1826–1831.
30. Lu, C.; Liu, E.; Li, Y.; Zhu, G.; Shao, Y. Design and Coupled Moisture–Thermal Transfer Simulation of Opposite Cross-Section Polyethylene Terephthalate Knitted Fabric with Hygroscopic Quick-Drying Capability. *Materials* **2024**, *17*, 4370. [CrossRef] [PubMed]
31. Yichen, D.; Zheng, D.; Guo, K.; Zou, H.; Du, Z. Modeling Heat and Moisture Transfer in Cylindrical Porous Media Fabrics: Influencing Factors and Structural Optimization. *Text. Res. J.* **2025**, *95*, 2152–2164. [CrossRef]
32. Taheri, M.; Vadood, M.; Johari, M.S. Investigating the Effect of Yarn Count and Twist Factor on the Packing Density and Wicking Height of Lyocell Ring-Spun Yarns. *Fibers Polym.* **2013**, *14*, 1548–1555. [CrossRef]
33. Datta Roy, M.; Chattopadhyay, R.; Sinha, S.K. Wicking performance of profiled fibre part A: Assessment of yarn. *J. Inst. Eng. (India) Ser. E* **2017**, *98*, 155–163. [CrossRef]
34. Anand, N.; Jasper, W.J.; DenHartog, E. Modeling heat transfer through Filament Yarns by Random Geometry. In Proceedings of the COMSOL Conference 2018, Boston, MA, USA, 3–5 October 2018.
35. Kumar, V.; Sampath, V.R.; Prakash, C. Investigation of stretch on air permeability of knitted fabrics part II: Effect of fabric structure. *J. Text. Inst.* **2016**, *107*, 1213–1222.
36. Troynikov, O.; Wardiningsih, W. Moisture management properties of wool/polyester and wool/bamboo knitted fabrics for the sportswear base layer. *Text. Res. J.* **2011**, *81*, 621–631. [CrossRef]

37. *Standard's ISO 11092:2014*; Textiles—Physiological Effects—Measurement of Thermal and Water-Vapour Resistance under Steady-State Conditions (Sweating Guarded-Hotplate Test). International Organization for Standardization: Geneva, Switzerland, 2014.
38. Alam, M.M.; Chowdhury, M.A.; Sabnam, E.J.; Islam, M.S. Improvement of Moisture Management of Polyester Fabric Using Moisture Management Chemical. *Int. J. Eng. Technol. Manag. Appl. Sci.* **2017**, *5*, 71–78.

Disclaimer/Publisher's Note: The statements, opinions and data contained in all publications are solely those of the individual author(s) and contributor(s) and not of MDPI and/or the editor(s). MDPI and/or the editor(s) disclaim responsibility for any injury to people or property resulting from any ideas, methods, instructions or products referred to in the content.